Enhancing comfort and efficiency in high-speed marine craft through active hydrofoil technology: A numerical comparison between foiling and planing hulls

Ocean Engineering 359 (2026) 125968

Contents lists available at ScienceDirect

Ocean Engineering

journal homepage: www.elsevier.com/locate/oceaneng

Research paper

Enhancing comfort and efficiency in high-speed marine craft through active hydrofoil technology: A numerical comparison between foiling and planing hulls

Francesco Balestrieri [a,*], Mauro Bonfanti [a], Marnix van Schrojenstein Lantman [b], Pietro Casalone [a], Eelco Frickel [b], Stefano Mauro [a], Luigi Francesco Minerva [b]

[a] Polytechnic University of Turin, Department of Mechanical and Aerospace Engineering, Turin, 10129, Italy
[b] Maritime Research Institute Netherlands, Wageningen, 6708 PM, The Netherlands

ARTICLE INFO

Keywords:
Hydrofoil
Planing hull
Seakeeping
Energy efficiency
Motion control

ABSTRACT

Hydrofoil-supported craft offer a promising alternative to conventional planing hulls, addressing critical limitations regarding seakeeping and hydrodynamic efficiency in rough seas. This study quantifies these performance benefits using a novel hybrid numerical framework that couples mid- and high-fidelity hydrodynamic models within a real-time simulation environment; The framework's novelty lies in calibrating computationally efficient models with pre-computed high-fidelity data. This approach enables the real-time simulation of complex hydrofoil dynamics in stochastic waves. The investigation compares a standard planing Rigid Hull Inflatable Boat against a retrofitted hydrofoil configuration controlled by a Sliding Mode Controller for active flap actuation. Simulations conducted across a range of irregular sea states demonstrate that the Sliding Mode Controller enables a 'platforming' mode, successfully filtering out wave-induced disturbances to maintain a stable flight altitude. This reduces vertical accelerations by an order of magnitude, which extends the ISO 2631-1 safe operational envelope from less than one hour (for the planing hull) to over four hours. Furthermore, in rougher sea states, the foiling configuration achieves a 60/90% increase in speed and a 40/50% reduction in fuel consumption relative to the planing baseline, effectively mitigating the speed degradation and increased power demand typically observed in planing hulls. These findings provide a quantitative basis for the adoption of active hydrofoil technology, highlighting its potential to enhance passenger comfort and support decarbonization efforts in high-speed maritime transport.

1. Introduction

High-speed marine craft are essential to modern shipping, serving key functions in passenger transport, defense, and logistics (The Maritime and Coastguard Agency, 2008; Balestrieri et al., 2025). While conventional planing hulls remain the industry standard due to their operational reliability at high Froude numbers, they are constrained by high vertical accelerations and substantial energy demands in rough sea states (Faltinsen, 2005; Olausson, 2015; Razola et al., 2016). These characteristics compromise passenger comfort and escalate operational costs. Consequently, as the maritime sector aims to meet rigorous decarbonization targets, enhancing hydrodynamic efficiency and seakeeping has become a critical objective in high-speed craft design (The marine environmental protecntion committee, 2018; Balestrieri et al., 2025).

Hydrofoil-supported craft have re-emerged as a compelling alternative to conventional planing vessels. By generating lift via submerged or semi-submerged foils, the hull is fully or partially emerged, resulting in reduced wetted surface area, mitigated drag, and enhanced seakeeping qualities (Hoerner et al., 1954; Michel et al., 1954; Molland and Turnock, 2022). Although extensive research has demonstrated improvements in resistance and ride quality across various operational conditions (Faltinsen, 2005; Hoerner et al., 1954; Milandri, 2006; Buermann, 1953), the practical implementation of foiling technology is complicated by highly nonlinear dynamics (Richard, 1962). These complexities arise primarily from unsteady fluid–structure interactions and the rigorous requirements for maintaining dynamic stability during flight in stochastic wave environments (Minerva et al., 2024; Seyfi and Nouri, 2020).

To facilitate performance prediction and design optimization, diverse experimental and numerical methods have been applied to

* Corresponding author.
E-mail address: francesco.balestrieri@polito.it (F. Balestrieri).

https://doi.org/10.1016/j.oceaneng.2026.125968
Received 17 February 2026; Received in revised form 17 April 2026; Accepted 6 May 2026

hydrofoil-assisted craft. Computational Fluid Dynamics (CFD) models provide detailed insight into flow structures and hydrodynamic loads (Niloy et al., 2022); however, their prohibitive computational cost often restricts their utility to targeted parametric studies of wing performance rather than comprehensive operational assessments (Pernod et al., 2022; Kumari et al., 2023). To overcome these computational bottlenecks, mid- and low-fidelity models for the simulation of hydrofoil wings have been widely utilized; these include Lifting Line Theory (LLT) (Godø et al., 2024), Vortex Lattice Methods (VLM) (van Walree, 1999), and Boundary Element Methods (BEM) (Perali et al., 2024; Bal and Kinnas, 2002). While these approaches significantly reduce calculation times, they often require robust semi-empirical corrections to accurately capture critical viscous phenomena, free-surface proximity effects, and cavitation. Furthermore, they may still fail to resolve essential nonlinear and transient dynamics (Hoerner et al., 1954; Michel et al., 1954; Godø et al., 2024; Minerva et al., 2024). Parallel to the developments in foil modeling, numerical methodologies for conventional high-speed craft have continuously advanced (Tavakoli et al., 2024). Although CFD simulations represent a valuable tool (Caponnetto et al., 2003), they impose a similarly high computational burden in this context. This limitation has driven the widespread adoption of $2D+t$ (two-dimensional plus time) strip theory to obtain reliable results through faster simulation frameworks (Kahramanoglu et al., 2021). By reducing complex 3D planing hydrodynamics into a sequence of unsteady 2D water-entry impacts, $2D+t$ methods offer computationally efficient yet highly accurate predictions of dynamic lift, 6DOF motions, and wave-induced slamming loads (Bonci and Marin, 2023). Consequently, hybrid approaches that synthesize this modeling technique with case-specific or generalized empirical corrections have proven valuable for efficiently assessing performance while preserving physical realism (Bonci and Marin, 2023).

The present work, a collaboration between the Maritime Research Institute Netherlands (MARIN) and the Polytechnic University of Turin, employs a hybrid numerical framework designed to analyze the dynamics of hydrofoil-supported and planing craft in irregular waves. This simulation environment integrates inputs from both mid-fidelity and high-fidelity hydrodynamic methods. Specifically, the framework utilizes pre-computed high-fidelity data to calibrate computationally efficient models, ensuring real-time execution capability without compromising the accuracy required for analyzing hydrofoil dynamics. Furthermore, a Sliding Mode Controller is implemented to actuate the hydrofoil flap incidence, thereby ensuring dynamic stability. This architecture facilitates a rigorous comparison between planing and hydrofoil-supported configurations under consistent control strategies and environmental conditions.

The primary objective of this research is to provide a quantitative benchmark comparing the performance of conventional planing hulls against actively controlled hydrofoil-supported configurations. Using consistent environmental inputs and control logic, the analysis evaluates two critical aspects:

- Seakeeping and Comfort: The study specifically quantifies the reduction in vertical accelerations, which are direct precursors to Motion Sickness Incidence (MSI) and crew fatigue (International Towing Tank Conference, 1999; Ente Italiano di Normazione, 1997).
- Energy Efficiency: The work estimates the potential reduction in propulsion power demand and fuel consumption, directly correlating these metrics to lower carbon emissions.

By establishing a rigorous comparison across diverse sea states, this work aims to substantiate the operational viability of hydrofoil technology as a cornerstone for sustainable high-speed maritime transport.

The remainder of this paper is structured as follows: Section 2 details the hybrid numerical architecture and the control laws governing the vessel; Section 3 defines the comparative metrics and operational scenarios; Section 4 analyzes the simulation data; and Section 5 offers concluding remarks and future outlooks.

2. Simulation framework and sliding mode control

The simulation framework, central to this investigation, is designed to conduct real-time analysis of marine vessels in generalized operational scenarios, yielding comprehensive data on system states and onboard dynamics. For the purpose of this study, a specific hull geometry serves as the test case, enabling a comparative performance analysis between a conventional planing configuration and a hydrofoil-supported variant.

2.1. Hydrodynamic modeling

The hydrodynamic model of the planing hull employs a $2D+t$ strip theory approach, utilizing a segmented geometric representation to balance accuracy with computational speed. The hull is discretized using a series of equally spaced transverse polygons (strips) arranged from aft to fore. At each simulation time step, the solver computes the instantaneous submergence and vertical velocity of each polygon. These kinematic inputs are used to calculate the localized hydrodynamic forces based on the semi-empirical methods detailed by Bonci and Marin (2023) and Frickel et al. (2021). This $2D+t$ strip theory representation allows for the rapid estimation of forces required for real-time applications while retaining sensitivity to hull geometry changes.

Modeling the hydrofoil-supported configuration introduces additional complexity due to the unsteady nature of foil loads (Minerva et al., 2024). To reconcile the requirement for high-fidelity load prediction with real-time execution constraints, the forces generated by the lifting surfaces are computed using a modified version of the unsteady aerodynamic model developed by the Institute of Aerodynamics and Gas Dynamics (IAG) at the University of Stuttgart. Originally proposed by Bangga et al. for wind turbine applications (Bangga et al., 2020, 2023), this formulation derives unsteady loads from steady-state solutions, thereby circumventing computationally expensive runtime evaluations. The steady-state input data is generated during a preprocessing phase, facilitating the integration of high-fidelity simulations or experimental results. The force coefficients are approximated via the following formulation:

$$\begin{aligned} C_l^D &= (C_n^f + C_n^V)\cos(\alpha) - C_t^V \sin(\alpha) \\ C_d^D &= (C_n^f + C_n^V)\sin(\alpha) + C_t^V \cos(\alpha) \end{aligned} \tag{1}$$

where C_l^D and C_d^D represent the dynamic lift and drag coefficients, respectively. C_n^f denotes the unsteady viscous normal force coefficient, C_n^V is the normal force contribution resulting from unsteady trailing edge vortex detachment, C_t^V is the unsteady viscous tangential force coefficient, and α is the angle of attack. These coefficients are derived by applying lag functions and force modifications to account for flow separation, as detailed in Bangga et al. (2020). In this work, minor modifications are introduced to C_n^f, which depends on the impulsive normal force coefficient. To ensure fidelity, a constant parameter within this formulation was calibrated to align the model's predictions with high-fidelity unsteady hydrofoil simulations across a spectrum of reduced frequencies.

Since the original IAG model is aerodynamic in nature, it inherently neglects hydrodynamic-specific phenomena such as phase changes and free-surface proximity. Assuming the principle of superposition holds for these hydrodynamic corrections, the final coefficients are formulated as:

$$\begin{aligned} C_l &= k_v \frac{C_l}{C_{l_\infty}} C_l^D \\ C_d &= C_d^D + C_{d_{strut}} + C_{d_{spray}} + C_{d_w} \end{aligned} \tag{2}$$

where k_v and C_l/C_{l_∞} represent the lift reduction induced by ventilation and/or cavitation and free-surface proximity, respectively. Furthermore, $C_{d_{strut}}$, $C_{d_{spray}}$, and C_{d_w} denote additional drag components associated with specific structural elements (such as the hydrofoil strut)

and physical phenomena (such as spray and wave generation). These individual correction terms are computed through the integration of several supplementary sub-models, which are detailed below:

- Cavitation and Ventilation: The integrity of the lifting flow is monitored by checking operation against pre-defined cavitation and ventilation boundaries calculated during pre-processing (Ng et al., 2025; Casey Mackenzie Harwood, 2016; Damley-Strnad et al., 2019; Harwood et al., 2014; Ferreira et al., 2025). If the foil state breaches these boundaries, a penalty function is triggered to simulate the sudden loss of lift associated with fluid phase change or air entrainment. Following the approach of Harwood (Casey Mackenzie Harwood, 2016; Damley-Strnad et al., 2019), the lift coefficient is scaled by a factor k_v (where $k_v = 1$ represents fully wetted flow). Fig. 1 shows the loss of lift due to ventilation or phase change. The sudden drop represents the "penalty function" triggered when the foil breaches ventilation boundaries.
- Strut and Spray Drag: Parasitic drag components arising from the strut structure and the associated spray generation are modeled using empirical formulations from Michel et al. (1954), Chapman (1971), and Oossanen (2018). These contributions are incorporated into the total drag computation via the additional terms $C_{d_{strut}}$ and $C_{d_{spray}}$.
- Free-Surface Effects: The proximity of the foil to the water surface alters the pressure field. This phenomenon is modeled here via a novel weighted-mean approach. This method synthesizes the formulations of Oossanen (2018) and Molland and Turnock (2022) for lift, and combines (Michel et al., 1954) and Molland and Turnock (2022) for drag. This hybrid lift model leverages the respective strengths of both formulations, as they exhibit optimal performance in distinct operational domains. Specifically, the van Oossanen approach captures potential lift enhancement at specific depth-Froude number combinations, while Molland's method provides a continuous formulation valid outside the van Oossanen boundaries. The resulting weighted-mean model exhibited superior agreement when validated against the results of Nicolas et al. (2023) and Pernod et al. (2022). These effects are represented by the lift reduction factor C_l/C_{l_∞} and the additional wave drag coefficient C_{d_w}.

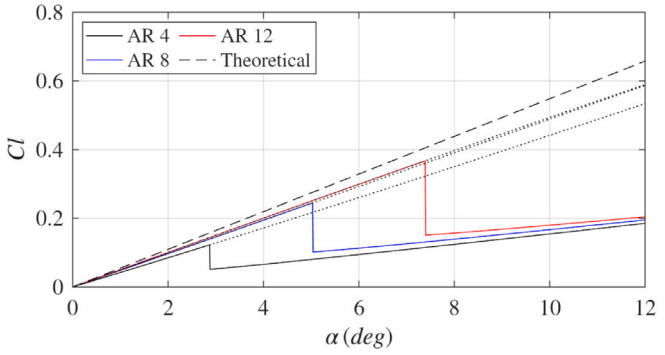

Fig. 1. Ventilation-induced lift reduction modeled across varying angles of attack for distinct aspect ratios (Casey Mackenzie Harwood, 2016).

Fig. 2 presents the validation of the lift coefficient ratio, C_l/C_{l_∞}, predicted by the adopted model against the benchmark data provided by Nicolas et al. (2023). The figure delineates the individual contributions of the underlying formulations: results derived from the van Oossanen approach (Oossanen, 2018) are depicted by black circles, while those corresponding to Molland and Turnock (2022) are represented by blue triangles. The proposed weighted-mean approach (red squares) is compared against the benchmark dataset (black dashed line), demonstrating the model's fidelity across the tested conditions.

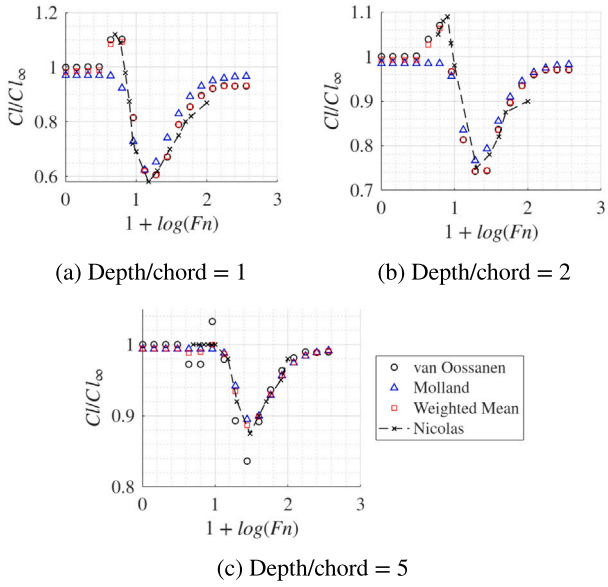

Fig. 2. Comparison of the adopted weighted-mean free-surface lift model against established literature for varying depth-to-chord ratios.

Fig. 2 also justifies the need for this complex model in the simulation, since lift coefficient losses, up to 40%, can be experienced in close to free-surface conditions.

Complementing this validation, Fig. 3 illustrates the application of the free surface model across the entire operational parameter space. This domain is defined by the specific combination of immersion depth (depth-to-chord ratio, d/c) and the Froude number function ($1 + \log(Fn)$). It confirms that free-surface effects (lift reduction) are most severe at shallow immersions (low d/c) and specific speeds. At high d/c, the foil behaves as if in infinite fluid ($Cl/Cl_\infty \approx 1$).

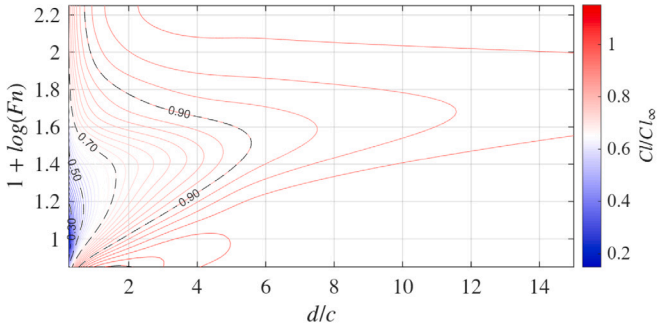

Fig. 3. Contour plot mapping the free-surface penalty on the lift coefficient (C_l/C_{l_∞}) across the operational domain. The parameter space is defined by the dimensionless immersion depth-to-chord ratio (d/c) and a logarithmic function of the Froude number ($1 + log(Fn)$).

2.2. Dynamic equations of motion

To simulate the vessel's dynamic behavior, a conventional six-degree-of-freedom (6-DoF) model is employed. The governing equations of motion are formulated in the body-fixed reference frame and are defined as:

$$(\mathbf{M} + \mathbf{M_a})\dot{\mathbf{v}}_\mathbf{b} + (\mathbf{C} + \mathbf{D})\mathbf{v}_\mathbf{b} = \boldsymbol{\tau} \tag{3}$$

In this formulation, $\mathbf{M}$ represents the rigid-body mass matrix, $\mathbf{M_a}$ denotes the hydrodynamic added mass, and $\mathbf{v_b}$ is the velocity vector (comprising linear and angular velocities), with $\dot{\mathbf{v}}_\mathbf{b}$ representing its time

derivative (linear and angular accelerations). Furthermore, $\mathbf{C}$ is the Coriolis matrix, $\mathbf{D}$ is the hydrodynamic damping matrix, and $\boldsymbol{\tau}$ is the resultant vector of all external forces and moments acting on the craft. For numerical implementation, these differential equations are discretized using a fourth-order Runge–Kutta integration scheme (Lindfield and Penny, 2012) with a time step of 1/60 s.

The external force vector, $\boldsymbol{\tau}$, is pivotal for modeling the craft's environmental interactions. While various decomposition methods exist (Fossen, 2011; Tristan, 2019), for the specific objectives of this study, the total force vector is partitioned into two primary components based on the generating surfaces, expressed mathematically as:

$$\boldsymbol{\tau} = \boldsymbol{\tau}_{hull} + \boldsymbol{\tau}_{wings} \tag{4}$$

Here, $\boldsymbol{\tau}_{hull}$ comprises forces and moments acting on the main planing hull, and $\boldsymbol{\tau}_{wings}$ comprises forces and moments generated exclusively by the hydrofoils. This decomposition is fundamental to the simulation architecture, creating a distinct interface for integrating unsteady hydrofoil loads into the primary planing hull model via a Functional Mock-up Unit (FMU). The hull forces, $\boldsymbol{\tau}_{hull}$, are computed within the main simulation environment, incorporating environmental loads such as wind and waves (Bonci and Marin, 2023; Frickel et al., 2021). Functionally, the hull load component can be described as $\boldsymbol{\tau}_{hull} = f_{hull}(\mathbf{v}_b, \boldsymbol{\eta}, \boldsymbol{\zeta}, \mathbf{V}_w)$, where $\boldsymbol{\eta}$ represents the global position and attitude, $\boldsymbol{\zeta}$ the wave elevation, and $\mathbf{V}_w$ the wind velocity. Conversely, the foil forces, $\boldsymbol{\tau}_{wings}$, are determined by a specialized independent process. This process accounts for the craft's attitude, accelerations, and active control system outputs, yielding a generalized functional form of $\boldsymbol{\tau}_{wings} = f_{wings}(\mathbf{v}_b, \dot{\mathbf{v}}_b, \boldsymbol{\eta}, \boldsymbol{\zeta}, \delta)$, where δ represents the active hydrofoil flap incidence angle. This architecture effectively decouples the hydrodynamic load computation of the planing hull model from the foiling subsystem, although the two components remain dynamically coupled via the rigid-body equations of motion. This modularity ensures a consistent comparison; the same hydrodynamic model employed for the planing hull is applied to the foiling craft. This model calculates relevant hull forces ($\boldsymbol{\tau}_{hull}$) during wetted phases and yields negligible forces when the hull is foil-borne. In the current simulator development stage, hydrodynamic interactions between the hull and hydrofoils are not explicitly modeled. While this simplification introduces a margin of error during pre-takeoff and transition, the effect becomes negligible once the vessel achieves a fully foil-borne state.

2.3. Flight control and telegraph strategy

The active stabilization of the hydrofoil configuration is achieved through a Sliding Mode Controller (SMC). This nonlinear control technique is widely recognized for its inherent robustness against external disturbances (Bartolini and Ferrara, 1996; Fossen and Foss, 1991), such as wave impacts, and its simplicity of tuning. SMC is utilized here as a pragmatic baseline strategy, facilitating a platforming mode (Faltinsen, 2005) without reliance on advanced sensing capabilities.

The fundamental principle of SMC is to drive the system's state trajectory onto a user-defined subspace within the state space, known as the sliding surface or sliding manifold. This surface is engineered such that when the system's state is on it, the system exhibits the desired behavior (e.g., stable tracking of a reference signal, regulation to zero). The control problem is thus divided into two phases: *reaching phase*, the controller applies a control action that forces the system's state trajectory to move from any initial position toward the sliding surface and *sliding phase*, once on the surface, the controller keeps the system state "sliding" along it, ensuring the desired system dynamics and robustness. The first step in SMC design is to define the sliding surface, $S(t)$, which mathematically represents the desired system dynamics. This is typically defined as a function of the system's tracking error, e, (the difference between the desired state and the actual state). The goal is to enforce the condition $s(x,t) = 0$, where s is the sliding variable. A common formulation for the sliding variable, which includes an integral term to eliminate steady-state errors, is a weighted sum of the tracking error, its derivatives, and its integral:

$$s = e^{(r-1)} + k_{r-1}e^{(r-2)} + \cdots + k_1 e + k_0 \int_0^t e\, d\tau \tag{5}$$

Here, e is the tracking error, $e^{(r-1)}$ is the $(r-1)$-th derivative of the error, and k_i are user-defined gains that determine the dynamics during the sliding phase. A practical implementation of this surface uses a first-order sliding variable (where the system relative degree $r = 2$). The sliding variable s is defined as a linear combination of the error e and its derivative $\dot{e}$: $s = \dot{e} + \lambda e$. In this context, the error vector e represents the deviation from the desired attitude, such as $e = [z - z_{ref}, \theta - \theta_{ref}]^T$, where z is the heave and θ is the pitch. The design matrix λ is chosen to define the stable error dynamics (i.e., how quickly the error decays) once the system is on the sliding surface. To make the sliding surface attractive and to keep the system on it, the control law incorporates a discontinuous term. A simplified conceptualization of the control law u is $u = u_{eq} + u_{disc}$ where u_{eq} is the equivalent control, a theoretical continuous control component required to maintain the state on the surface ($s = 0$) assuming a perfect model and u_{disc} is the discontinuous control, a switching component that ensures the system reaches the surface and compensates for any model uncertainties or disturbances. This discontinuous term is defined using the $sign$ function:

$$u_{disc} = -k \cdot sign(s) \tag{6}$$

Where k is a positive gain. This high-speed switching action constantly forces the system trajectory back toward the $s = 0$ manifold, effectively trapping it there and making the system's behavior independent of (or robust to) any bounded disturbances that are weaker than the control gain k. A major practical drawback of the pure SMC is the infinite-frequency switching of the $sign(s)$ function. This phenomenon, known as *chattering*, can excite unmodeled high-frequency dynamics in the system and cause physical wear or damage to actuators. To mitigate chattering, the discontinuous $sign(s)$ function is typically replaced by a continuous, high-gain approximation within a thin boundary layer, ϵ, around the sliding surface. This quasi-sliding control law smooths the control action near the surface, eliminating chattering at the cost of a small, bounded tracking error instead of perfect tracking.

Complementing the flight control, a standardized telegraph control logic was implemented to ensure comparable test conditions between the foiling and planing configurations. The telegraph was calibrated using baseline simulations in calm water (see Section 3.2), yielding two discrete settings: mid and high power levels (Fig. 4). These settings correspond to steady-state speeds of approximately $0.55V_{max_{planing}}$ and $0.85V_{max_{planing}}$, respectively, for both configurations. For the planing configuration, the telegraph remains constant throughout the simulation. However, the foiling configuration required a modified logic to standardize the transition phase. Relying solely on the final target telegraph from the simulation onset resulted in highly variable times-to-takeoff and, in some instances, failure to achieve liftoff due to the

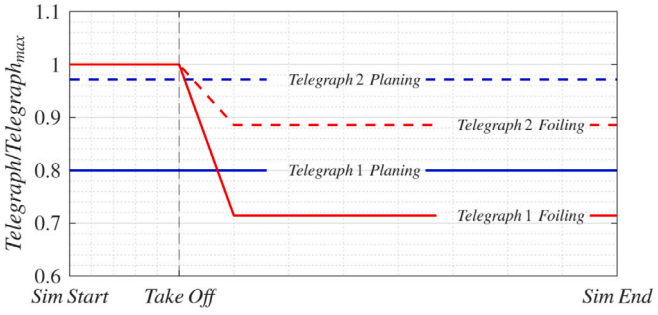

Fig. 4. Standardized telegraph settings normalized to the maximum telegraph considered for both foiling and planing configuration.

(a) Standard planing hull

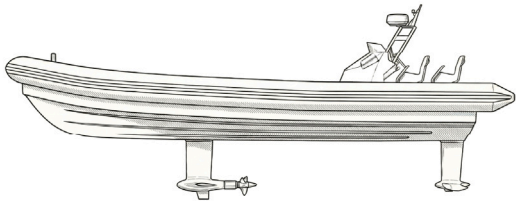

(b) Retrofitted hydrofoil configuration

Fig. 5. Schematic representations of the baseline rigid hull inflatable boat (RHIB) configurations.

critical takeoff speed requirement of $\sim 0.25 V_{max_{planing}}$. To address this, a constant initial telegraph is applied, specifically calibrated to ensure the craft reaches takeoff speed within a narrow, sea state-dependent time window. Upon takeoff, this initial telegraph is linearly reduced to the target value required for the desired steady-state speed. This strategy ensures successful takeoff across all tested sea states and maintains a consistent transition duration. Subsequently, a buffer period allows the foiling configuration to stabilize in its steady-state regime before data sampling commences. This logic is illustrated in Fig. 4. Notably, the foiling craft's final telegraph setting is lower than that of the planing craft, providing an initial indication of the reduced power requirements for maintaining steady-state speed.

3. Comparative methodology: vessel configurations, evaluation criteria, baseline performance and environmental conditions

The comparative analysis employs a Rigid Hull Inflatable Boat (RHIB) as the baseline platform (Fig. 5). This vessel features a deep-V hull geometry with an overall length of approximately 10 m, a beam of $\sim$ 3 m and a draft of $\sim$ 1 m. Further detailed measurements cannot be disclosed due to confidentiality restrictions. This specific hull geometry was selected because its planing characteristics have been previously detailed and validated within the MARIN simulation environment (Bonci and Marin, 2023). Starting from this baseline, two distinct configurations were established:

1. Planing: The baseline RHIB hull operating in its standard hydrodynamic mode.
2. Foiling: The baseline hull retrofitted with a hydrofoil subsystem. The lifting surfaces consist of two T-shaped foils in a conventional non-split arrangement (Faltinsen, 2005). Modeled as rigid bodies, the wings feature a taper ratio of 1.0 (rectangular planform) and zero twist. Their surface areas and longitudinal positions are sized to support the vessel's displacement while ensuring dynamic stability with zero dynamic trim (Fig. 5).

3.1. Metrics for comparative performance analysis

To rigorously quantify the comparative operational performance of the two configurations, three primary performance domains were defined: velocity degradation, energy efficiency, and ride quality.

Speed is utilized as a primary performance metric because simulations are conducted with a fixed telegraph setting. Consequently, while the power input remains constant, the resulting vessel speed varies significantly due to added wave resistance. This metric quantifies the speed loss induced by the sea state. To facilitate comparison across different telegraph settings and configurations, we define a dimensionless speed-keeping index, denoted as Φ. This parameter normalizes the time-averaged longitudinal speed attained in waves against its corresponding calm-water baseline value:

$$\Phi = \frac{1}{V_{x,\,calm\,water}} \left[\frac{1}{t_e - t_0} \int_{t_0}^{t_e} V_x(t)\, dt \right] \tag{7}$$

where t_0 and t_e denote the start and end of the sampling interval, respectively. Consequently, a value of $\Phi = 1$ indicates zero speed penalty, while progressively lower values directly quantify the velocity degradation imposed by the environmental conditions.

The propulsive cost is assessed via fuel consumption. This metric serves as a direct indicator of efficiency, defined here as the specific fuel consumption per unit distance: $\psi(t) = r(t)/V_x(t)$, where $r(t)$ is the fuel mass flow rate (kg/s) and $V_x(t)$ is the vessel speed (m/s). To ensure comparability between planing and foiling configurations across different operational points, this metric is normalized against the consumption rate recorded in the corresponding calm water conditions:

$$\Psi = \frac{1}{\psi_{calm\,water}} \left[\frac{1}{t_e - t_0} \int_{t_0}^{t_e} \psi(t)\, dt \right] \tag{8}$$

Crucially, the fuel consumption rate, $r(t)$, is computed as a function of the instantaneous power delivered by the engine, thereby dynamically reflecting wave interactions and the complete system dynamics. The engine and propeller characteristics are modeled using performance maps derived from the specific unit installed on the test RHIB; consequently, these data cannot be disclosed due to confidentiality restrictions.

Finally, the accelerations ($a_x(t)$ and $a_z(t)$) measured at the center of gravity constitute the primary metric for seakeeping quality in this specific study. These values quantify the degree of hydrodynamic coupling between the vessel and the free surface: high magnitudes indicate strong coupling, whereas low values demonstrate effective decoupling. Beyond structural dynamics, acceleration is the critical determinant of human factors, driving Motion Sickness Incidence (MSI) models (O'Hanlon and Mccauley, 1974; Piscopo and Scamardella, 2015) and the ISO 2631-1 comfort standards (Ente Italiano di Normazione, 1997).

Fig. 6 depicts the ISO 2631-1 *health caution zone*, which relates the root mean square (RMS) of the weighted acceleration magnitude (a_w) to permissible exposure limits. This zone delineates safe operation (falling below Zones 1 and 2) from potential health risks (exceeding Zones 1 and 2). To compute the instantaneous weighted accelerations, $a^*_{w,i}(t)$, the raw acceleration signals ($a_i(t)$) are processed through a transfer function $H_i(p)$ that simulates the human body's frequency-dependent sensitivity to vibration. This transfer function is composed of a cascade of filters:

$$H_i(p) = H_{h,i}(p) H_{l,i}(p) H_{t,i}(p) H_{s,i}(p) \tag{9}$$

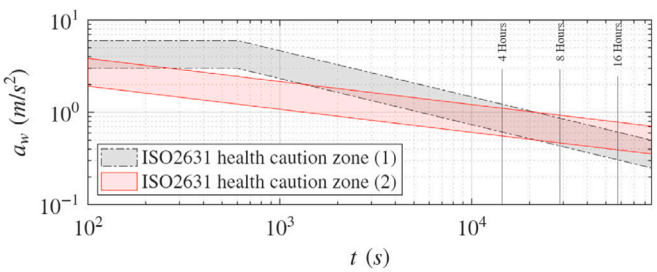

Fig. 6. ISO 2631-1 health caution zones correlating the root-mean-square of the weighted acceleration magnitude (a_w) to permissible exposure limits.

Specifically, the chain includes high-pass ($H_{h,i}$) and low-pass ($H_{l,i}$) band-limiting filters, a transition filter ($H_{t,i}$), and a specific impact response filter ($H_{s,i}$). The transfer functions for the longitudinal (x) and vertical (z) directions, denoted as H_x and H_z respectively, are defined by the standard and illustrated in Fig. 7.

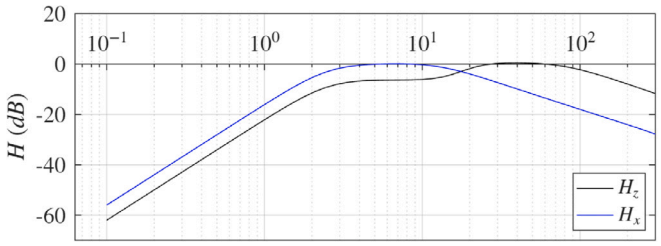

Fig. 7. Frequency-dependent acceleration transfer functions defined by the ISO 2631-1 standard.

Following the weighting process, the RMS of the weighted accelerations is computed as:

$$a_{w,i} = \sqrt{\frac{1}{t_e - t_0}\int_{t_0}^{t_e} a_{w,i}^{*}(t)^2\, dt} \tag{10}$$

To quantify the aggregate effect of accelerations across all three orthogonal axes, ISO 2631-1 defines the total weighted acceleration value (a_v):

$$a_v = \sqrt{(k_x a_{w,x})^2 + (k_y a_{w,y})^2 + (k_z a_{w,z})^2} \tag{11}$$

where k_x, k_y, k_z are direction-specific weighting factors defined by the standard.

The standard further establishes indices to assess onboard comfort regarding vibration. This study considers the estimated Vibration Dose Value ($eVDV = 1.4 a_w T^{1/4}$) (Ente Italiano di Normazione, 1997), the Motion Sickness Dose Value ($MSDV_z$) (Ente Italiano di Normazione, 1997), and the Motion Sickness Incidence (MSI) index (Ente Italiano di Normazione, 1997). It is important to distinguish the specific definitions of MSI. Conventional models, such as those adopted by O'Hanlon and Mccauley (1974) and Piscopo and Scamardella (2015), define MSI as the percentage of exposed personnel likely to vomit within 2 h of exposure to specific vertical accelerations. Conversely, ISO 2631-1 estimates the percentage of people expected to vomit by relying on the $MSDV_z$ (measured in $m/s^{1.5}$) to quantify exposure over the measurement period. The Motion Sickness Dose Value is calculated as:

$$MSDV_z = \sqrt{\int_{t_0}^{t_e} a_w(t)^2\, dt} \tag{12}$$

The corresponding Motion Sickness Incidence is then derived as:

$$MSI = K_m MSDV_z \tag{13}$$

where K_m is a constant reflecting the susceptibility of the exposed population; it is set to 1/3 in this analysis to represent a mixed population (male and female) unadapted to the vibration environment.

3.2. Calm-water baseline performance

The performance baseline was established by deriving calm water resistance curves for both configurations across the full range of available telegraph settings. Fig. 8 illustrates the normalized drag ($D/D_{max_{planing}}$) and velocity ($V/V_{max_{planing}}$) profiles.

The hydrodynamic behavior in calm water reveals a fundamental distinction: the planing hull exhibits a characteristic "hump" in resistance as it transitions to planing mode. Conversely, the hydrofoil configuration demonstrates a drastic reduction in drag once the takeoff

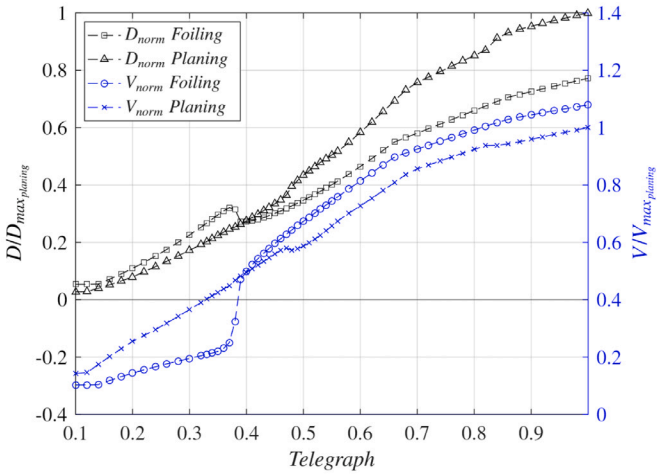

Fig. 8. Calm water hydrodynamic performance curves detailing normalized drag, $D/D_{max_{planing}}$, and velocity, $V/V_{max_{planing}}$, profiles as a function of the telegraph setting.

threshold is surpassed ($Telegraph > 0.35$). This bifurcation allows the foiling craft to achieve significantly higher velocities for equivalent power inputs, quantifying the efficiency gains derived from eliminating the hull's wetted surface area.

Figs. 9 and 10 show the power benefits of the foiling configuration relative to the planing baseline. Specifically, Fig. 9 presents the power requirements for both vessels, normalized against the maximum power and speed of the planing configuration. The normalized effective delivered power curve (Balestrieri et al., 2025), denoted as $P/P_{max_{planing}}$, shows that hydrofoils yield a substantial reduction in power demand at high speeds, enabling the attainment of higher velocities for the same delivered power. Moreover, the planing configuration curve clearly identifies the location of the previously cited drag hump; indeed, at approximately 60% of its maximum speed, the effective delivered power curve rises steeply without a corresponding increase in speed, indicating a local increase in hydrodynamic drag.

Furthermore, Fig. 10 illustrates the power ratio between the foiling and planing configurations. This comparison confirms that in the displacement mode (below takeoff speed), the foiling craft is less efficient due to the added drag of the submerged appendages; however, once foilborne, it becomes significantly more efficient and capable of higher operational speeds.

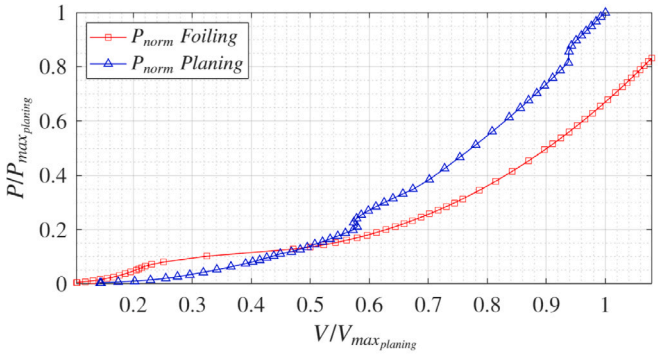

Fig. 9. Normalized delivered power ($P/P_{max_{planing}}$) as a function of normalized speed for the calm-water baseline.

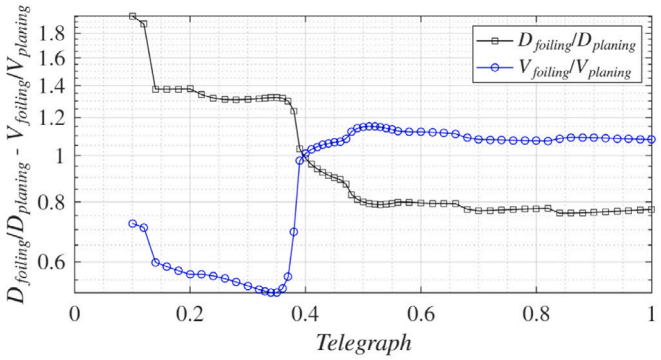

Fig. 10. Relative calm-water performance ratios between the foiling and planing configurations.

3.3. Irregular seaway test matrix

While the calm water results align with established literature (Faltinsen, 2005; Hoerner et al., 1954; Buermann, 1953), they neglect environmental disturbances, which are ubiquitous in operational profiles. To extend the analysis to realistic conditions, simulations were conducted in irregular waves ranging from calm to slight sea states (codes 0 to 3), which encompass approximately 45% of global operating conditions (Fossen, 2011).

The upper limit of the tested sea states was determined by geometric constraints. The strut length of the foil configuration is approximately equal to the maximum expected wave height in the $H_s = 1.0\,\text{m}$ sea state, inclusive of a safety margin equivalent to the hydrofoil's mean chord depth. This constraint prevents hull slamming or ventilation events caused by the foil breaching the free surface. The irregular wave fields were generated using a JONSWAP spectrum (Holthuijsen, 2007; Bonfanti et al., 2024). A comprehensive test matrix comprising 80 simulations per configuration was executed. This parametric sweep evaluated combinations of two wave peak periods (2.75 s and 3.5 s) and twenty wave heights, ranging from 0.05 m to 1.0 m in increments of 0.05 m.

4. Performance evaluation: seakeeping capabilities, energy efficiency, and passenger comfort

The results are evaluated using the metrics defined in Section 3.1 and are presented as a function of significant wave height (H_s), wave peak period (T_w), and telegraph setting. The data presented in the subsequent plots are derived exclusively from the steady-state regime, omitting the initial transient response.

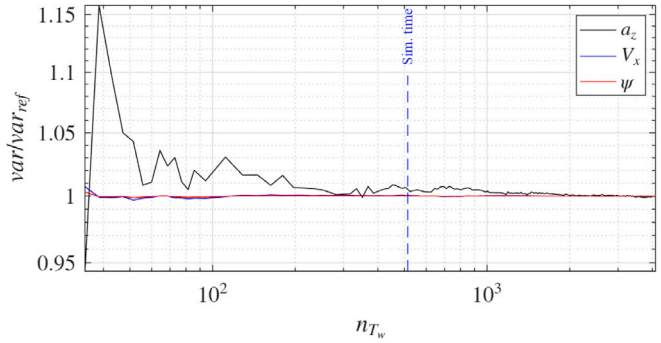

Fig. 11. Convergence analysis depicting the absolute relative error of primary state variables against a four-hour reference simulation.

Fig. 11 presents the three primary parameters normalized by the results of a 4-hour reference simulation, plotted as a function of the number of wave periods (n_{T_w}). After 30 min of simulation, corresponding to over 500 periods for the longest wave period (T_w) analyzed, the ratio consistently remains below 1.01 for all variables. Consequently, a duration of 30 min was selected for the subsequent analysis, as this interval is sufficient to ensure statistical convergence.

To provide a comprehensive view of the dynamic differences between the two configurations, Fig. 12 presents a comparative time-history extract. This dataset corresponds to a simulation in irregular waves with $H_s = 0.5$ m and $T_w = 2.75$ s, utilizing Telegraph 2 (high-speed setting). The results are divided into two distinct temporal phases: the transient phase ($t = 0$ s to 55 s) and the regime phase ($t = 500$ s to 550 s). During the transient, the foiling craft (red line) undergoes a transition phase where the initial constant telegraph accelerates the vessel to the takeoff velocity ($\approx 0.25V_{max}$). Upon checking the flight altitude, a clear departure from the water surface is visible at $t \approx 20$ s. Following this transition, the vertical position of the Center of Gravity, z, ascends to converge with the mean flight altitude, $\bar{z}$, which corresponds to the reference setpoint arbitrary defined by the controller. Conversely, the planing hull (blue line) remains surface-bound, exhibiting larger vertical oscillations immediately upon interacting with the wave field. The steady-state (regime) window ($t >$ 500 s) highlights the decoupling capability of the hydrofoil system:

- The foiling craft maintains a stable flight altitude with minimal deviation, whereas the planing hull tracks the wave elevation, resulting in continuous heave motion.
- The foiling craft maintains a normalized speed near 1.0 (calm water speed), while the planing hull suffers a speed degradation of approximately 40 – 50% due to waves.
- Longitudinal accelerations are an order of magnitude lower than vertical accelerations; therefore, although they are accounted for in this study, their contribution to the acceleration-related indices is negligible.
- The planing hull vertical acceleration signal is characterized by high-frequency, high-amplitude spikes indicative of slamming events (a_z frequently exceeding 4 m/s^2). In contrast, the foiling signal is smooth and of low amplitude, validating the effectiveness of the Sliding Mode Controller in attenuating wave-induced disturbances.

Fig. 12(e) presents data specific to the flying configuration, illustrating the time history of the controlled flap incidence. These results demonstrate the controller's effectiveness in maintaining the dynamic stability of the craft. Notably, a distinct disparity is observed in the actuation of the respective foils. While optimizing this actuation strategy lies beyond the scope of this study, it represents a promising avenue for future research to further reduce vertical acceleration and minimize power usage. Finally, as specific details regarding the actuation system are not disclosed and its impact varies significantly between implementations, the energy consumed by the actuators is excluded from the overall energy analysis.

The shaded regions accompanying the curves in Figs. 13 to 15 denote the 2% and 98% quantiles of the recorded time-series data. These bands characterize the temporal variability of the respective parameters throughout the simulation.

Fig. 13 presents the normalized longitudinal speed (Φ), quantifying the speed-keeping capability of both configurations. The speed of the planing craft degrades significantly with increasing significant wave height (H_s), indicating a severe penalty due to added wave resistance. In contrast, the foiling craft's speed remains nearly independent of H_s, maintaining values close to calm-water performance. Additionally, the wider shaded regions (representing the 2% and 98% quantiles) for the planing hull indicate higher speed variability. When comparing Fig. 13(a) (Telegraph 1) to Fig. 13(b) (Telegraph 2), the foiling craft exhibits no distinct differences beyond a marginal reduction in speed loss. However, the planing configuration demonstrates a shift in the critical speed drop: for Telegraph 1, this drop occurs between $H_s = 0.3$

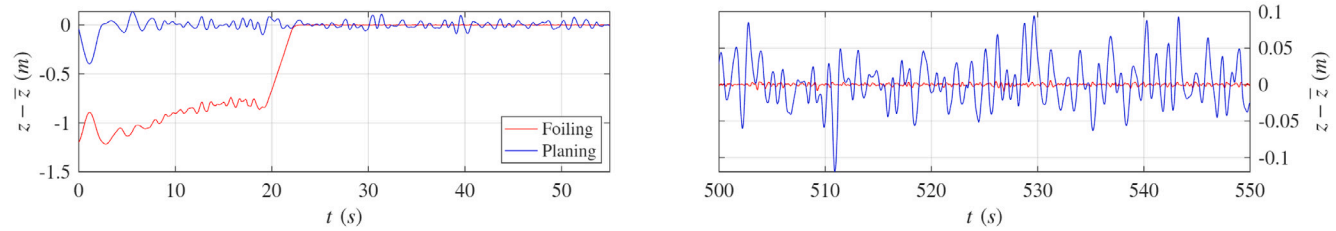

(a) Craft vertical positions (z) minus regime mean vertical positions ($\overline{z}$)

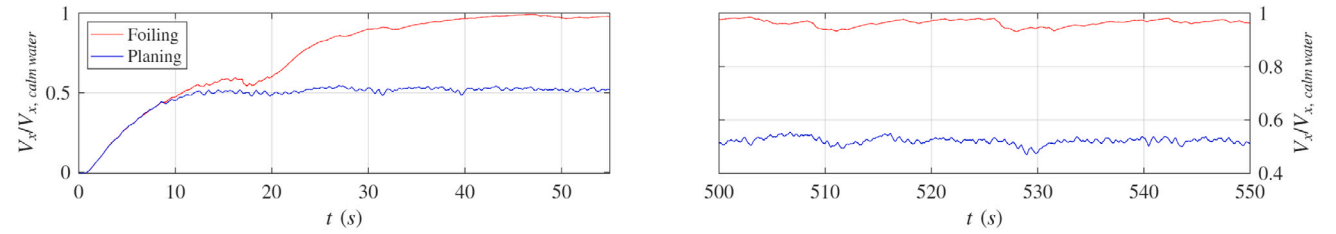

(b) Craft normalised speeds

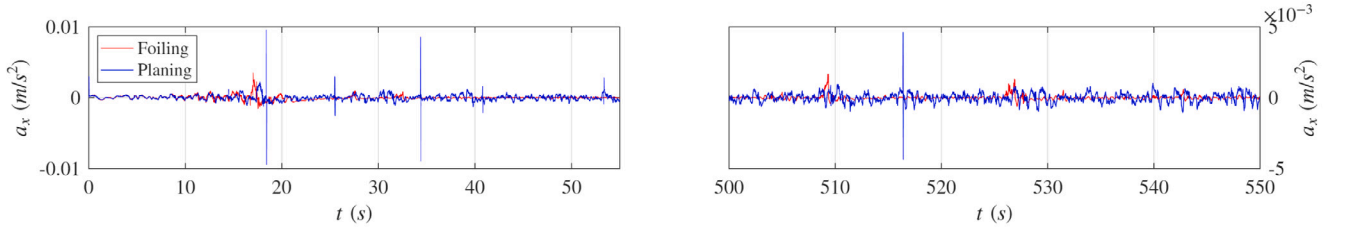

(c) Craft longitudinal accelerations

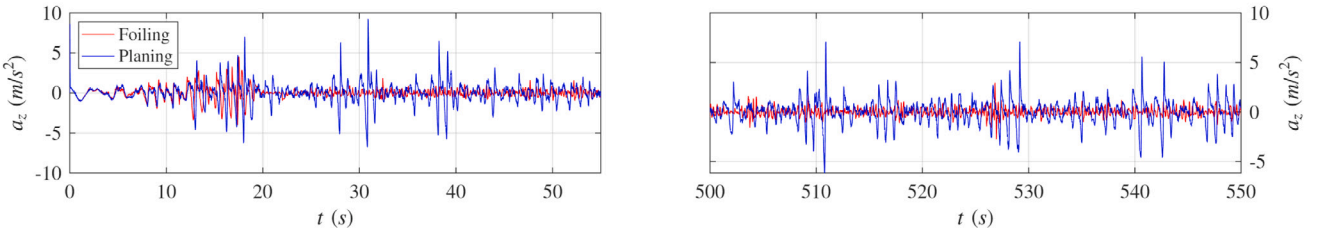

(d) Craft vertical accelerations

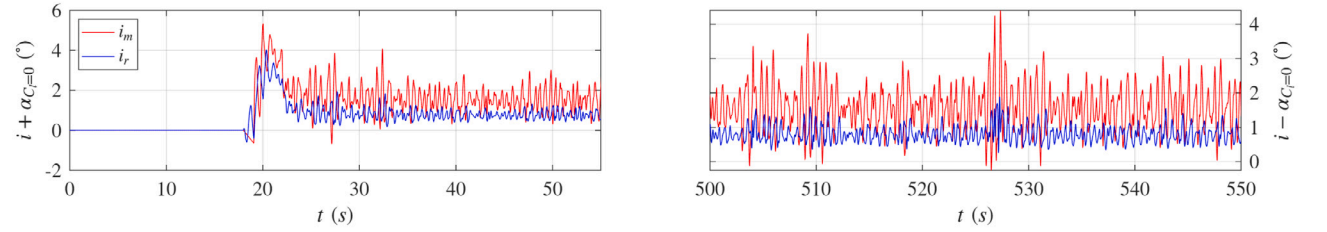

(e) Foiling configuration, hydrofoil incidence control actuation

Fig. 12. Comparative time-history of vessel dynamics during transient ($t = 0 - 50$ s) and steady-state ($t = 500 - 550$ s) phases in an irregular sea state ($H_s = 0.5$ m, $T_w = 2.75$ s).

and 0.5, whereas for Telegraph 2, it shifts to the range of 0.75 to 1. This behavior is likely attributable to the vessel's operating point relative to the drag hump (as highlighted in the calm-water performance, Fig. 8). At the higher telegraph setting, the craft operates well beyond the drag hump; consequently, it can sustain a larger increase in wave-induced resistance before decelerating back into the high-drag transition region. This confirms that by lifting the hull above the free surface, the hydrofoil configuration effectively circumvents the wave resistance penalty.

Fig. 14 plots the normalized mean specific fuel consumption (Ψ) against H_s, serving as the primary metric for energy efficiency. The planing craft's fuel requirement increases substantially (by 30 – 50%) with increasing H_s, a direct consequence of the additional power required to overcome wave-induced resistance. Consistent with the velocity analysis, a comparison of Fig. 14(a) and Fig. 14(b) reveals a distinct shift in the consumption trend governed by the vessel's proximity to the drag hump, a phenomenon observed exclusively in the planing configuration. In contrast, the foiling craft's consumption

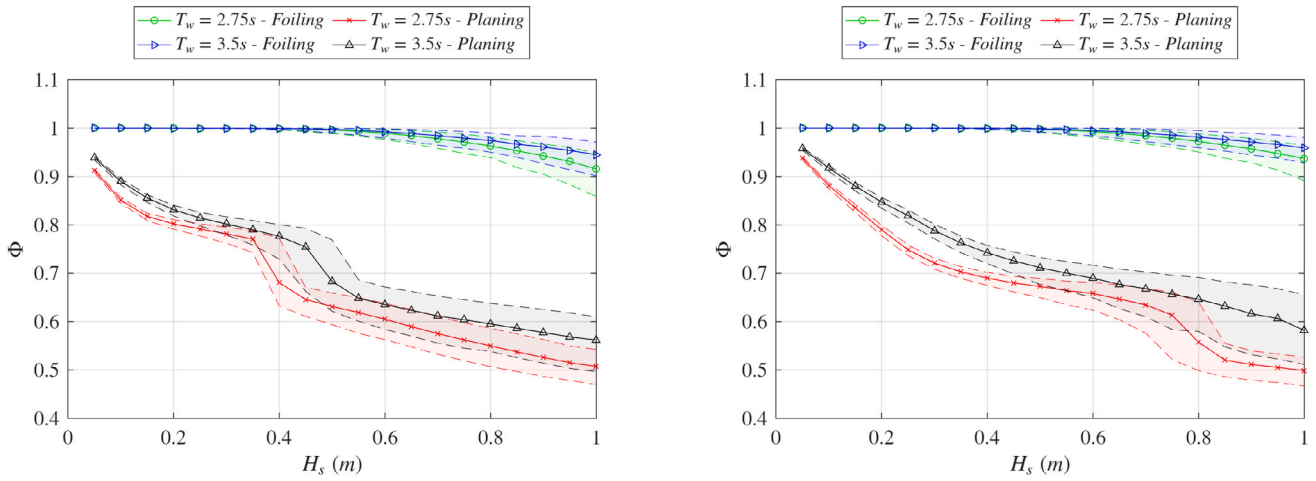

(a) Telegraph 1 (b) Telegraph 2

Fig. 13. Dimensionless speed-keeping index (Φ) as a function of significant wave height (H_s) for different telegraph settings and wave periods.

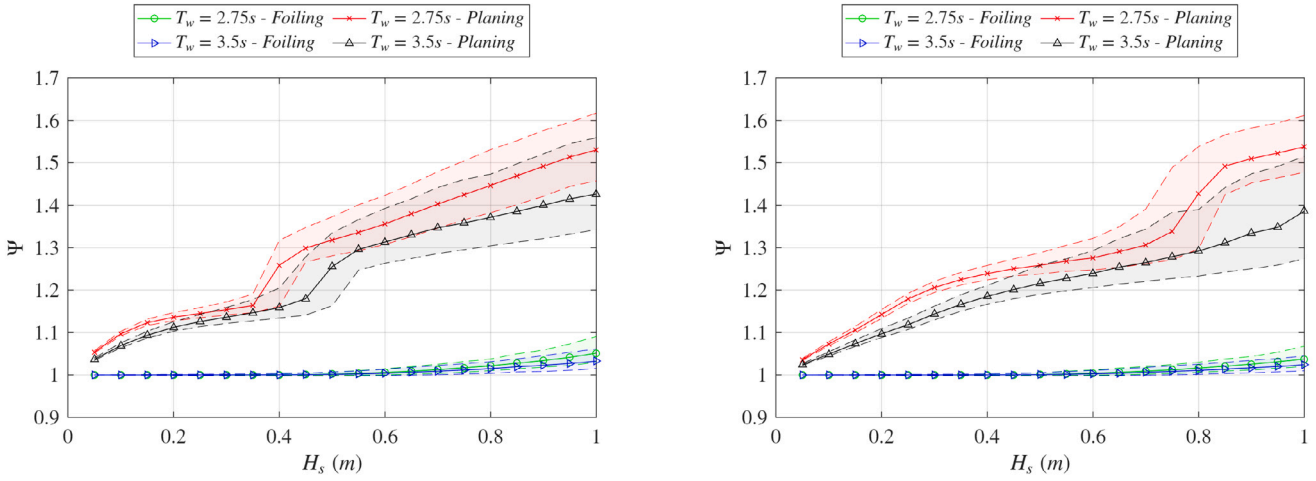

(a) Telegraph 1 (b) Telegraph 2

Fig. 14. Normalized mean specific fuel consumption (Ψ) evaluated across varying significant wave heights (H_s) and wave periods.

remains almost constant, deviating little from its calm-water baseline. This behavior reflects the fundamental efficiency advantage of hydrofoiling: by lifting the hull, the vessel substantially reduces its wetted surface area. This reduction mitigates the frictional contribution to total drag and minimizes wave-making resistance, directly translating into significant fuel savings. However, as previously noted, these specific propulsive savings must be contextualized by the exclusion of the energy required to actuate the hydrofoil control system, which would partially reduce the calculated margin of efficiency.

Fig. 15 presents the root-mean-square of vertical acceleration ($\widetilde{a}_z$), computed as:

$$\widetilde{a}_z = \sqrt{\frac{1}{t_e - t_0}\int_{t_0}^{t_e} a_z(t)^2\, dt} \tag{14}$$

and as a function of H_s for all test cases, it serves as the primary metric for seakeeping performance and passenger comfort. A pronounced disparity in acceleration magnitude is evident: the foiling craft's $\widetilde{a}_z$ is exceptionally low (maximum ~ 0.5 m/s^2) and exhibits only a marginal increase with H_s. Conversely, the planing craft's $\widetilde{a}_z$ is an order of magnitude higher (maximum $\sim 2-4$ m/s^2) and increases almost linearly with wave height. Comparing Fig. 15(a) to Fig. 15(b), it is observed that acceleration magnitudes scale with the telegraph setting, a result consistent with physical expectations. Furthermore, a critical distinction appears regarding the wave period: while the $\widetilde{a}_z$ of the planing configuration demonstrates sensitivity to the wave period, the hydrofoiling configuration appears largely independent of this parameter. This insensitivity is evidenced by the fact that the data curves for the foiling craft collapse onto a single trend across all sea states, regardless of the wave period. This behavior further underscores the superior seakeeping capabilities of the hydrofoil configuration.

To facilitate a direct comparison between the hydrofoil and planing configurations, Fig. 16 illustrates the relative variation of the performance parameters (Φ, Ψ, and $\widetilde{a}_z$) of the foiling craft compared to the planing hull. The trends for speed and consumption are consistent and distinct; conversely, the acceleration performance exhibits greater sensitivity to the wave period and telegraph setting. Notably, in rougher sea states, the hydrofoil configuration simultaneously achieves a 60 – 90% increase in speed and a 40 – 50% reduction in fuel consumption, all while significantly mitigating vertical accelerations.

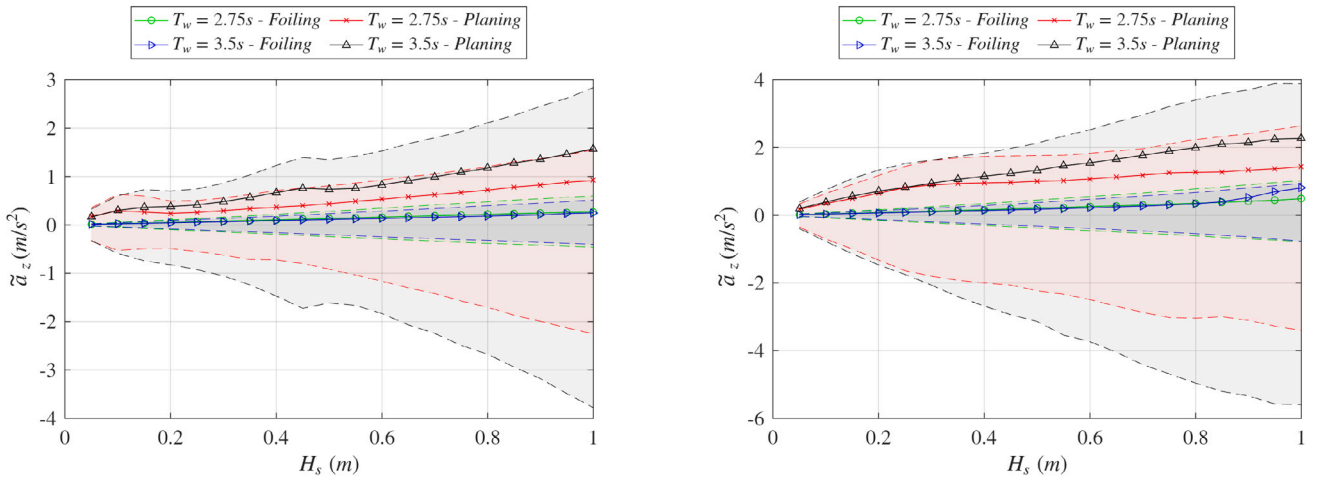

(a) Telegraph 1 (b) Telegraph 2

Fig. 15. Root-mean-square of vertical acceleration ($\tilde{a}_z$) as a function of significant wave height for distinct telegraph settings.

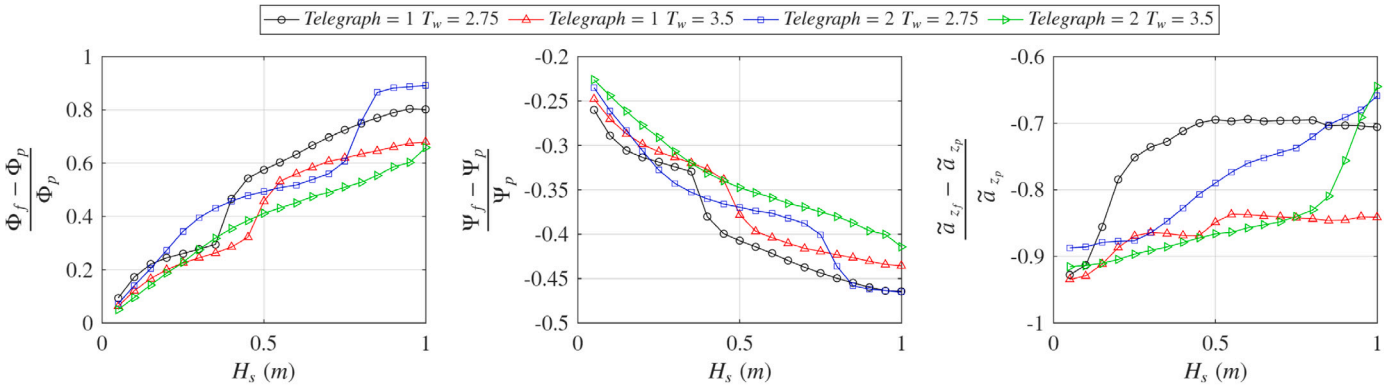

Fig. 16. Relative variance of speed-keeping, specific fuel consumption, and vertical acceleration performance of the hydrofoil configuration compared to the planing baseline. The comparative metrics are plotted against significant wave height for selected telegraph and wave period combinations.

As previously established, acceleration is the primary metric for assessing onboard comfort, in accordance with ISO 2631-1 (Ente Italiano di Normazione, 1997) and established literature (O'Hanlon and Mccauley, 1974; Piscopo and Scamardella, 2015). The following results are calculated using the methodology detailed in Section 3.1 and are evaluated against the limits illustrated in Fig. 6. It is important to note that while the standard defines two Health Guidance Caution Zones based on distinct formulations, this analysis adopts the strictest boundary corresponding to the computed acceleration magnitude. Given that continuous operations rarely exceed 24 h and the standard does not define limits beyond this duration, a 24-hour interval is adopted as the maximum upper bound for permissible acceleration exposure. However, as illustrated in Fig. 17, for certain lower acceleration magnitudes, the theoretical permissible exposure limit extends significantly beyond this 24-hour threshold.

Fig. 17 presents the simulation results distinguished by configuration: planing (red triangles) and foiling (blue circles). Notably, the data corresponding to the foiling configuration cluster to the right of the limitation boundaries. This distribution indicates a substantially longer permissible exposure duration for the hydrofoil, consistent with its lower associated weighted acceleration levels.

Fig. 18 presents the projected maximum allowable exposure time. This graph directly corresponds to Fig. 17, depicting the same dataset across different axes. It quantifies the duration for which the computed

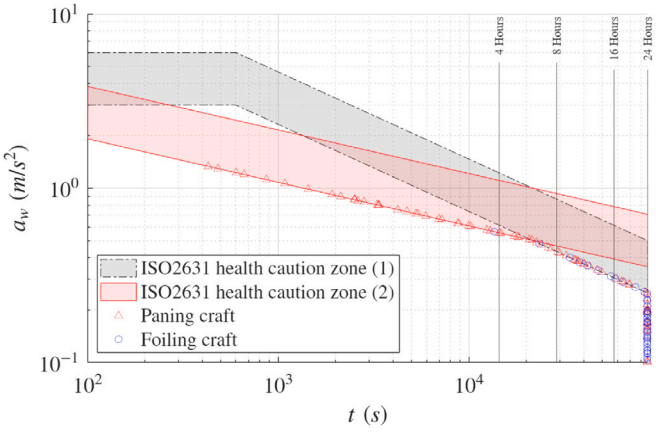

Fig. 17. Computed frequency-weighted RMS vertical accelerations mapped against the permissible exposure limits defined by the ISO 2631-1 standard.

frequency-weighted RMS acceleration can be sustained before breaching the standard's health caution zone. The results indicate that the planing craft (red and green lines) faces severe operational limitations; specifically, at high telegraph settings and increased wave heights,

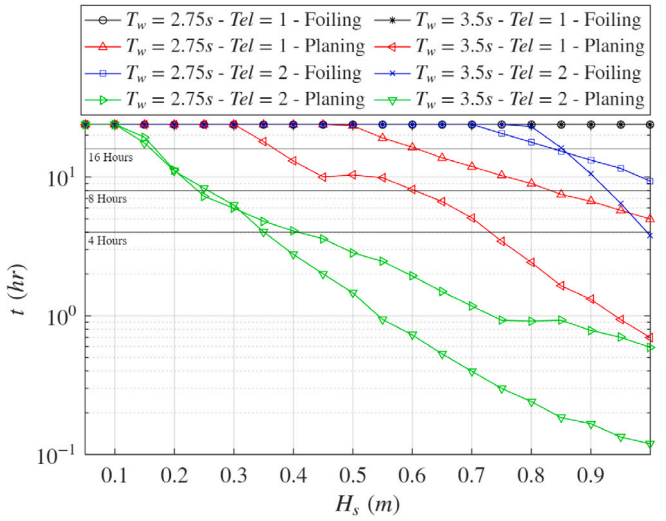

Fig. 18. Projected maximum allowable exposure time as a function of significant wave height before breaching the ISO 2631-1 health caution threshold.

the permissible exposure time drops to less than one hour. In contrast, the foiling craft (blue and black lines) maintains safe operation for durations exceeding 4 h across nearly the entire tested range. This demonstrates a significant expansion of the vessel's operational envelope regarding crew and passenger well-being.

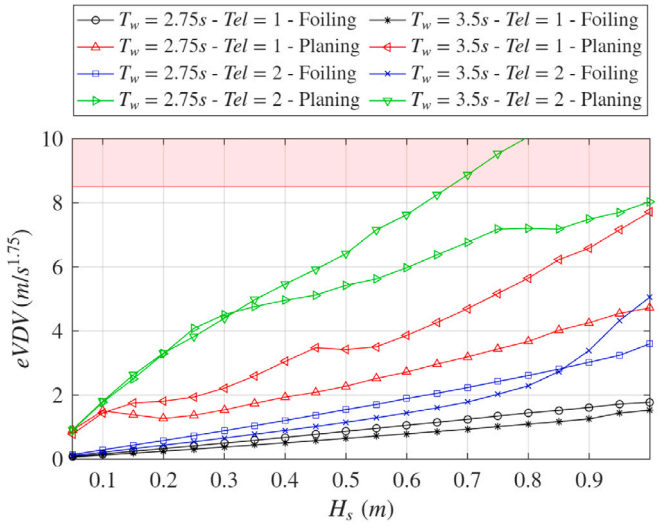

Fig. 19. Estimated Vibration Dose Value (eVDV) distributions evaluated across the simulated significant wave heights.

Fig. 19 presents the data for the estimated Vibration Dose Value. According to Ente Italiano di Normazione (1997), the initial health caution threshold is set at 8.5 $m/s^{1.75}$, which corresponds to the lower boundary of the red health caution zone illustrated in Fig. 6. The hydrofoil configuration consistently exhibits $eVDV$ values that are less than half those of the planing configuration under identical conditions. Furthermore, for a wide range of tested conditions, the $eVDV$ trend for the hydrofoil is nearly linear. This behavior is a direct consequence of the acceleration trends illustrated in Fig. 15 and is further corroborated by the data in Fig. 20.

Fig. 20 illustrates the Motion Sickness Incidence as a function of significant wave height (H_s). The MSI is quantified as a probability index (ranging from 0 to 1.0), representing the likelihood of passengers experiencing seasickness during the exposure period. The trends distinguished by these data are unequivocal. The planing craft (red and green lines) exhibits a notable risk of motion sickness, reaching incidence rates of 10 – 20% in moderate sea states. In sharp contrast, the foiling craft (blue and black lines) generally maintains an MSI below 5% across the majority of tested conditions, with maximum values restricted to 7.73%. This outcome is a direct consequence of the active control system's capability to attenuate the specific vertical acceleration frequencies that drive motion sickness. Consequently, this characteristic serves as a critical performance differentiator for commercial passenger transport applications.

Table 1 quantifies the performance disparity between the hydrofoil-supported configuration and the conventional planing hull across the tested operational envelopes. Consistent with the trends illustrated in the preceding figures, this performance gap widens as sea states deteriorate. For instance, in a sea state characterized by $H_s = 1.0$ m and $T_w = 3.5$ s with the telegraph set to its maximum value, the hydrofoil exhibits a marginal speed reduction of approximately 4% relative to calm water conditions. Conversely, the planing hull suffers a severe reduction of nearly 40%. Simultaneously, the hydrofoil maintains superior ride quality, subjecting passengers to vertical accelerations that are approximately one-third of the magnitude recorded for the planing configuration.

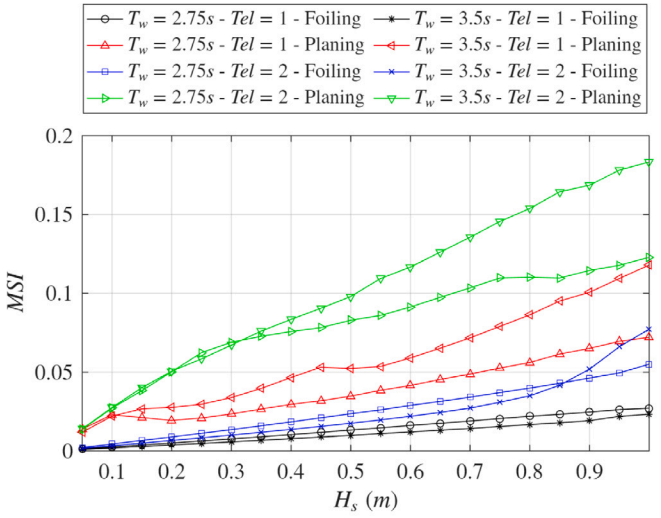

Fig. 20. Probability index for the Motion Sickness Incidence (MSI) as a function of significant wave height.

To summarize the findings, Table 2 presents the maximum, minimum, and mean values of the performance ratios between the foiling and planing configurations across all tested conditions. The data consistently demonstrate the superiority of the hydrofoil configuration across all considered indicators. Crucially, these ratios are derived from variables normalized against each vessel's respective calm-water performance. Therefore, rather than a simple comparison of absolute magnitudes, these values quantify the relative degradation of performance compared to calm water conditions. Even within this normalized framework, the results unequivocally highlight the superior robustness of the foiling craft. Note that in the table, the subscript f denotes the foiling configuration, while the subscript p indicates the planing one.

5. Conclusion

This study, conducted in collaboration between MARIN and the Polytechnic University of Turin, employed a hybrid numerical framework to provide a definitive quantitative assessment of the operational benefits of active hydrofoil technology. By subjecting identical hull geometries, one planing and one foil-supported, to a systematic test matrix of irregular sea states, the research isolated the specific advantages

Table 1
Extract of the comparative results between foiling and planing configuration.

$Telegraph\,1 \quad - \quad T_w = 2.75\,s$												
H_s	Foiling						Planing					
	$\Phi - 1$ (%)	$\Psi - 1$ (%)	$\widetilde{a}_w$ (m/s^2)	$eVDV$ (m/s$^{1.75}$)	t (h)	MSI (%)	$\Phi - 1$ (%)	$\Psi - 1$ (%)	$\widetilde{a}_w$ (m/s^2)	$eVDV$ (m/s$^{1.75}$)	t (h)	MSI (%)
0.10	−0.003	0.001	0.026	0.162	24.000	0.25	−14.875	9.686	0.294	1.507	24.000	2.30
0.25	−0.022	0.005	0.065	0.413	24.000	0.63	−20.831	14.473	0.260	1.368	24.000	2.09
0.40	−0.086	0.030	0.105	0.678	24.000	1.04	−31.950	25.836	0.365	1.935	24.000	2.96
0.55	−0.642	0.344	0.147	0.959	24.000	1.47	−38.127	33.597	0.487	2.516	19.146	3.85
0.70	−2.176	1.242	0.190	1.243	24.000	1.90	−42.460	40.245	0.626	3.190	11.912	4.88
0.85	−4.690	2.756	0.232	1.521	24.000	2.33	−46.239	46.947	0.782	4.020	7.501	6.15
1.00	−8.443	5.131	0.270	1.775	24.000	2.71	−49.261	53.033	0.919	4.717	4.980	7.21
$Telegraph\,1 \quad - \quad T_w = 3.5\,s$												
H_s	Foiling						Planing					
	$\Phi - 1$ (%)	$\Psi - 1$ (%)	$\widetilde{a}_w$ (m/s^2)	$eVDV$ (m/s$^{1.75}$)	t (h)	MSI (%)	$\Phi - 1$ (%)	$\Psi - 1$ (%)	$\widetilde{a}_w$ (m/s^2)	$eVDV$ (m/s$^{1.75}$)	t (h)	MSI (%)
0.10	−0.005	0.002	0.021	0.123	24.000	0.19	−10.984	6.881	0.302	1.445	24.000	2.21
0.25	−0.029	0.010	0.054	0.311	24.000	0.47	−18.548	12.562	0.414	1.938	24.000	2.96
0.40	−0.085	0.032	0.088	0.508	24.000	0.78	−22.371	15.855	0.670	3.047	13.058	4.66
0.55	−0.437	0.226	0.123	0.720	24.000	1.10	−35.136	29.585	0.755	3.504	9.874	5.36
0.70	−1.558	0.878	0.159	0.932	24.000	1.43	−38.831	34.677	0.995	4.692	5.085	7.17
0.85	−3.318	1.923	0.197	1.170	24.000	1.79	−41.367	38.564	1.279	6.221	1.646	9.51
1.00	−5.479	3.239	0.250	1.527	24.000	2.33	−43.804	42.643	1.571	7.712	0.697	11.79
$Telegraph\,2 \quad - \quad T_w = 2.75\,s$												
H_s	Foiling						Planing					
	$\Phi - 1$ (%)	$\Psi - 1$ (%)	$\widetilde{a}_w$ (m/s^2)	$eVDV$ (m/s$^{1.75}$)	t (h)	MSI (%)	$\Phi - 1$ (%)	$\Psi - 1$ (%)	$\widetilde{a}_w$ (m/s^2)	$eVDV$ (m/s$^{1.75}$)	t (h)	MSI (%)
0.10	−0.001	0.000	0.040	0.288	24.000	0.44	−11.842	7.263	0.347	1.777	24.000	2.72
0.25	−0.006	−0.002	0.100	0.732	24.000	1.12	−25.142	17.908	0.813	4.080	7.280	6.24
0.40	−0.036	0.006	0.165	1.206	24.000	1.84	−31.000	23.881	0.954	4.956	4.086	7.58
0.55	−0.407	0.216	0.232	1.705	24.000	2.61	−33.567	26.845	1.024	5.622	2.467	8.60
0.70	−1.564	0.896	0.303	2.232	24.000	3.41	−36.527	30.632	1.185	6.766	1.176	10.34
0.85	−3.514	2.057	0.382	2.809	15.362	4.29	−47.963	49.237	1.280	7.176	0.929	10.97
1.00	−6.249	3.733	0.487	3.599	9.358	5.50	−50.141	53.766	1.429	8.035	0.591	12.28
$Telegraph\,2 \quad - \quad T_w = 3.5\,s$												
H_s	Foiling						Planing					
	$\Phi - 1$ (%)	$\Psi - 1$ (%)	$\widetilde{a}_w$ (m/s^2)	$eVDV$ (m/s$^{1.75}$)	t (h)	MSI (%)	$\Phi - 1$ (%)	$\Psi - 1$ (%)	$\widetilde{a}_w$ (m/s^2)	$eVDV$ (m/s$^{1.75}$)	t (h)	MSI (%)
0.10	−0.002	0.000	0.034	0.215	24.000	0.33	−8.229	4.876	0.389	1.803	24.000	2.76
0.25	−0.010	0.001	0.085	0.545	24.000	0.83	−18.052	11.819	0.823	3.822	8.298	5.84
0.40	−0.038	0.010	0.139	0.895	24.000	1.37	−25.776	18.511	1.153	5.460	2.773	8.35
0.55	−0.303	0.157	0.199	1.288	24.000	1.97	−29.969	22.779	1.458	7.156	0.940	10.94
0.70	−1.077	0.608	0.269	1.780	24.000	2.72	−33.211	26.492	1.772	8.870	0.398	13.56
0.85	−2.336	1.352	0.399	2.729	16.281	4.17	−36.775	31.110	2.098	10.751	0.185	16.44
1.00	−4.089	2.402	0.806	5.053	3.781	7.73	−41.819	38.588	2.271	11.991	0.119	18.33

Table 2
Mean values of performance degradation factors relative to calm-water baselines ratios for all tested sea states.

	$\frac{V_{x,f}}{V_{x,p}} - 1$ (%)	$\frac{\widetilde{a}_{z,f}}{\widetilde{a}_{z,p}} - 1$ (%)	$\frac{\psi_f}{\psi_p} - 1$ (%)	$\frac{t_e}{t_p} - 1$ (‰)	$\frac{MSI_f}{MSI_p} - 1$ (%)
$Mean$	46.23	−80.93	−36.51	1.16	−75.43
Max	89.18	−64.50	−22.61	9.51	−55.21
Min	5.05	−93.48	−46.53	0.00	−92.10

provided by active flight control, confirming that hydrofoil adoption offers distinct performance gains over traditional designs.

The implementation of a Sliding Mode Controller allowed the hydrofoil craft to achieve a "platforming" mode, effectively decoupling the hull from the free surface even in stochastic wave environments. The simulation data revealed that this decoupling resulted in vertical accelerations that were consistently an order of magnitude lower than those of the planing hull, effectively eliminating the high-frequency slamming events that characterize the planing regime in rough water. This drastic reduction in vertical motion validates the active control strategy's capability to filter out wave-induced disturbances, maintaining a stable flight altitude with minimal deviation.

These dynamic improvements directly translate into significant benefits in terms of human factors and operational safety. According to ISO 2631-1 standards, the planing craft's operation at high speed was limited to under 1 h in moderate seas due to health risks associated with vibration and shock, whereas the foiling craft remained within safe exposure limits for over 4 h, essentially expanding the vessel's operational envelope. Additionally, the active filtering of specific wave frequencies resulted in a Motion Sickness Incidence (MSI) of lower than 7.5%, a strong contrast to the almost 20% sickness probability observed in the planing configuration, thereby proving the technology's value for passenger comfort.

Finally, the study highlighted critical advantages in energy efficiency and environmental sustainability. The planing hull demonstrated a steep penalty in power demand as wave height increased, fighting against added wave resistance, while the foiling craft maintained speed and consumption rates comparable to its calm-water performance. This confirms that hydrofoil technology is a robust pathway for reducing fuel consumption and associated carbon emissions in real-world conditions.

Despite these promising results, certain limitations of the current numerical framework must be acknowledged, which concomitantly

define avenues for future research. Primarily, the present energy analysis excludes the power consumption required by the active control actuators; future studies should integrate actuator dynamics to provide a holistic assessment of the net efficiency gains. Furthermore, the hydrodynamic interactions between the hull and the hydrofoil subsystems are not explicitly modeled. While this simplification is justifiable for the fully foil-borne regime, incorporating these coupled interaction effects will be crucial for a more accurate resolution of the transient takeoff phase. Additionally, the lifting surfaces are currently evaluated as rigid bodies; integrating hydroelastic effects could enhance the fidelity of unsteady load predictions in rougher sea states. Finally, although the Sliding Mode Controller provided a highly robust baseline strategy, future work should explore advanced optimization of the actuation strategy to further minimize required control effort and refine passenger comfort.

Collectively, these findings validate the utility of real-time hybrid numerical tools for complex vessel design and support the maritime industry's transition toward more efficient, safe, and comfortable high-speed transport solutions.

CRediT authorship contribution statement

Francesco Balestrieri: Writing – review & editing, Writing – original draft, Visualization, Software, Methodology, Investigation, Formal analysis, Data curation, Conceptualization. **Mauro Bonfanti:** Writing – review & editing, Supervision, Methodology, Formal analysis, Conceptualization. **Marnix van Schrojenstein Lantman:** Writing – review & editing, Supervision, Software, Methodology, Conceptualization. **Pietro Casalone:** Writing – review & editing, Supervision. **Eelco Frickel:** Writing – review & editing, Supervision. **Stefano Mauro:** Writing – review & editing, Supervision. **Luigi Francesco Minerva:** Writing – review & editing, Supervision, Project administration, Methodology, Conceptualization.

Funding

This research was funded by the Italian Ministry of University and Research (MUR) under the program DM 117/2023.

Declaration of competing interest

The authors declare that they have no known competing financial interests or personal relationships that could have appeared to influence the work reported in this paper.

Acknowledgments

The authors would like to express their sincere gratitude to MARIN and Polytechnic University of Turin for their joint support and collaboration throughout the development and execution of this study. Special thanks are extended to the technical and research teams involved in the simulation and analysis activities for their valuable contributions.

References

Bal, S., Kinnas, S.A., 2002. A BEM for the prediction of free surface effects on cavitating hydrofoils. Comput. Mech. 28, 260–274.

Balestrieri, Francesco, Brusasco, Alessandro, Melchiorre, Matteo, Bonfanti, Mauro, Mauro, Stefano, 2025. Methodological framework for assessing the sustainability of electric passenger fleets: Application to the egadi archipelago. Appl. Energy 401.

Bangga, G., Lutz, T., Arnold, M., 2020. An improved second-order dynamic stall model for wind turbine airfoils. Wind. Energy Sci. 5 (3), 1037–1058.

Bangga, G., Parkinson, S., Collier, W., 2023. Development and validation of the IAG dynamic stall model in state-space representation for wind turbine airfoils. Energies 16 (10).

Bartolini, Giorgio, Ferrara, Antonella, 1996. Multi-input sliding mode control of a class of uncertain nonlinear systems. IEEE Trans. Autom. Control 41.

Bonci, Matteo, Marin, Pepijn De Jong, 2023. High-speed RHIB seakeeping analysis using non-linear time domain simulations and systematic hull parametrization. Prog. Mar. Sci. Technol. 11–22.

Bonfanti, Mauro, Faedo, Nicolás, Mattiazzo, Giuliana, 2024. Towards efficient control synthesis for nonlinear wave energy conversion systems: impedance-matching meets the spectral-domain. Nonlinear Dynam. 112 (13), 11085–11109.

Buermann, T.M., 1953. An Appraisal of Hydrofoil Supported Craft. The Society of Naval Architects and Marine Engineers, New York.

Caponnetto, Mario, Söding, Heinrich, Azcueta, Rodrigo, 2003. Motion simulations for planing boats in waves. Ship Technol. Res. 50 (4), 182–198.

Casey Mackenzie Harwood, 2016. The Hydrodynamic and Hydroelastic Responses of Rigid and Flexible Surface-Piercing Hydrofoils in Multi-Phase Flows (Ph.D. thesis). The University of Michigan.

Chapman, Richard B., 1971. Spray Drag of Surface-Piercing Struts. Technical Report, Naval undersea research and development center, San Diego.

Damley-Strnad, Alexandra, Harwood, Casey M., Young, Yin Lu, 2019. Hydrodynamic performance and hysteresis response of hydrofoils in ventilated flows. In: Sixth International Symposium on Marine Propulsors. Rome, Italy.

Ente Italiano di Normazione, 1997. UNI ISO 2631-1. Technical Report, UNI.

Faltinsen, Odd M., 2005. Hydrodynamics of high-speed marine vehicles. Cambridge University Press.

Ferreira, Manuel Aguiar, Rodríguez, Carlos Navas, Jacobi, Gunnar, Fiscaletti, Daniele, Greidanus, Arnoud, Westerweel, Jerry, 2025. On the ventilation of surface-piercing hydrofoils under steady-state conditions.

Fossen, Thor I., 2011. Handbook of Marine Craft Hydrodynamics and Motion Control. Wiley, p. 596.

Fossen, Thor I., Foss, Bjarne A., 1991. Sliding control of MIMO nonlinear system. Model. Identif. Control 12, 129–138.

Frickel, Eelco, Schrijvers, Patrick, Mostert, Erik, Sovilj, Vladimir, 2021. Wind modelling sensitivity on free-fall lifeboat simulations. In: International Ocean and Polar Engineering Conference, The 31st International Ocean and Polar Engineering Conference, ISOPE–I–21–3170.

Godø, John Martin Kleven, Steen, Sverre, Faltinsen, Odd Magnus, 2024. A resistance model for hydrofoil fast ferries with fully submerged foil systems. Ocean Eng. 301.

Harwood, Casey M., Montero, Francisco Miguel, Young, Yin Lu, 2014. Experimental and numerical investigation of ventilation inception and washout mechanisms of a surface-piercing hydrofoil. In: 30th Symposium on Naval Hydrodynamics. Hobart, Tasmania, Australia.

Hoerner, S.F., Michel, W.H., Ward, L.W., Buermann, T.M., 1954. Hydrofoil Handbook Vol.I - Design Od Hydrofoil Craft. Technical Report, Naval Reserch Navy Department, Washington, D.C.

Holthuijsen, Leo H., 2007. Waves in Oceanic and Coastal Waters. Cambridge University Press.

International Towing Tank Conference, 1999. ITTC-Recommended Procedures and Guidelines. Excerpt of ISO 2631, Seasickness and Fatigue. Technical Report, ITTC.

Kahramanoglu, Emre, Pennino, Silvia, Yilmaz, Huseyin, 2021. Numerical evaluation of hydrodynamic characteristics of planing hulls by using a hybrid method. Proc. Inst. Mech. Eng. Part M: J. Eng. Marit. Environ. 235 (2), 344–355.

Kumari, Nutan, Chakraborty, Arnab, Jangam, Suneela, 2023. The hydrodynamic analysis of multiple hydrofoils translating in tandem in presence of a free surface. Proc. Inst. Mech. Eng. Part M: J. Eng. Marit. Environ. 237, 1008–1026.

Lindfield, G.R., Penny, J.E.T., 2012. Numerical Methods Using MATLAB, third ed. Elsevier.

Michel, W.H., Hoerner, S.F., Ward, L.W., Buermann, T.M., 1954. Hydrofoil Handbook Vol.II - Hydrodynamic Characteristics of Components. Technical Report, Naval Reserch Navy Department, Washington, D.C.

Milandri, Giovanni Sergio, 2006. Seakeeping Control of HYSUCATs (Ph.D. thesis). University of Stellenbosch.

Minerva, Luigi Francesco, Odendaal, Kirsten, Marelli, Giancarlo, Scholcz, Thomas, 2024. Early design of hydrofoils: Foil design JIP overview and methods. In: 28th International HISWA Symposium.

Molland, Anthony F., Turnock, Stephen R., 2022. Marine rudders, hydrofoils and control surfaces, second ed. Matthew Deans.

Ng, Galen W., Yildirim, Anil, Lamkin, Andrew, Jonsson, Eirikur, Martins, Joaquim R.A., 2025. Design optimization of America's cup AC75 hydrofoil sections with flaps. J. Sail. Technol. 10, 50–73.

Nicolas, Hugo, Perali, Paolo, Sacher, Matthieu, Bot, Patrick, 2023. Boundary element method analysis of 3D effects and free-surface proximity on hydrofoil lift and drag coefficients in varied operating conditions. J. Sail. Technol. 8, 183–199.

Niloy, Rounak Saha, Dipto, Mohammed Jubair, Hassan, Mirza Md. Mehedi, 2022. Hydrodynamic performance analysis of hydrofoil supported high-speed vessel using computational fluid dynamics. MARTEC, The International Conference on Marine Technology, Dhaka.

O'Hanlon, James F., Mccauley, Michael E., 1974. Motion sickness incidence as a function of the frequency and acceleration of vertical sinusoidal motion. Aerosp. Med.

Olausson, Katrin, 2015. On Evaluation and Modelling of Human Exposure to Vibration and Shock on Planing High-Speed Craft (Ph.D. thesis). KTH - Royal Institute of Technology, Stockholm, Sweden.

Oossanen, Peter van, 2018. The science of sailing: Part 4, first ed. Van Oossanen Academy Publishers.

Perali, Paolo, Sacher, Matthieu, Leroux, Jean Baptiste, Wackers, Jeroen, Augier, Benoît, Hauville, Frédéric, Bot, Patrick, 2024. Performance prediction of a hydrofoil near the free surface using low (BEM) and high (RANS) fidelity methods. Appl. Ocean Res. 151.

Pernod, Laetitia, Sacher, Matthieu, Wackers, Jeroen, Augier, Benoit, Bot, Patrick, 2022. Free-surface effects on two-dimensional hydrofoils by RANS-VOF simulations. SNAME 24th Chesapeake Sailing Yacht Symposium.

Piscopo, Vincenzo, Scamardella, Antonio, 2015. The overall motion sickness incidence applied to catamarans. Int. J. Nav. Archit. Ocean. Eng. 7, 655–669.

Razola, Mikael, Olausson, Katrin, Garme, Karl, Rosén, Anders, 2016. On high-speed craft acceleration statistics. Ocean Eng. 114, 115–133.

Richard, Bernicker, 1962. Hydrofoil motion in irregular seas. Technical Report, Davidson Laboratory.

Seyfi, Siamak, Nouri, Nowrouz Mohammad, 2020. Experimental studies of hysteresis behavior of partial cavitation around NACA0015 hydrofoil. Ocean Eng. 217.

Tavakoli, Sasan, Zhang, Mingyang, Kondratenko, Aleksander A., Hirdaris, Spyros, 2024. A review on the hydrodynamics of planing hulls. Ocean Eng. 303.

The marine environmental protecntion committee, 2018. Initial IMO Strategy on Reduction of GHG Emissions from Ships. Technical Report, International Maritime Organisation.

The Maritime and Coastguard Agency, 2008. International Code of Safety for High-Speed Craft. Technical Report, The Maritime and Coastguard Agency.

Tristan, Perez, 2019. Ship Motion Control: Course Keeping and Roll Stabilisation Using Rudder and Fins. Springer.

van Walree, Frans, 1999. Computational Methods for Hydrofoil Craft in Steady and Unsteady Flow (Ph.D. thesis). Technische Universiteit Delft.